RSC Advances

ROYAL SOCIETY OF CHEMISTRY

www.rsc.org/advances

Journal Name

ARTICLE

Nanoflake Driven Mn$_2$O$_3$ Microcubes Modified with Cooked Rice Derived Carbon for Improved Electrochemical Behavior

B. Chandra Sekhar [a], Ganguli Babu [b] and N. Kalaiselvi [a*]

Abstract: Mn$_2$O$_3$ microcubes, symmetrically formed out of the systematic stacking of nanoflakes, built with nanoparticles in the 30-50 nm range have been obtained from a simple co-precipitation method. Excluding the requirement of a structure directing additive, the currently adopted synthesis protocol signifies the vital role of rate of (NH$_4$)HCO$_3$ precursor addition, which has been optimized as 2 h for 300 mL to obtain uniformly stacked nanoflakes of Mn$_2$O$_3$ to form microcubes with desired morphological feature. Cooked rice carbon (CRC), obtained from a filth-to-wealth conversion has been used as conducting additive and an optimum concentration of 20 wt% CRC was found to be sufficient to form Mn$_2$O$_3$/CRC with improved lithium intercalation/ de-intercalation behavior. The twin advantages, namely exploitation of a cheap and eco-benign composite additive obtained from a common domestic waste in the form of CRC and the optimized speed of addition of (NH$_4$)HCO$_3$ to form Mn$_2$O$_3$ microcubes obtained from nanoflakes offer advantages in terms of enhanced electronic conductivity and provision to buffer the volume changes of Mn$_2$O$_3$ anode respectively. The optimized Mn$_2$O$_3$/CRC-20 composite anode exhibits an appreciable capacity of 830 mA h g^{-1} after formation cycle and an acceptable capacity of 490 mA h g^{-1} after completing 100 cycles, under the influence of 50 mA g^{-1} current density. Further, Mn$_2$O$_3$/CRC-20 anode exhibits a reasonable capacity of 450 mA h g^{-1} at 100 mA g^{-1} up to 50 cycles and qualifies itself as a potential anode material.

1. Introduction

Rechargeable lithium-ion batteries, bestowed with high voltage, capacity and appreciable cycle life are considered as one of the most promising electrochemical power sources, as they are widely used in many portable applications such as mobile phones, laptops and cameras. It is well known that a combination of all the desired properties in one electrode is generally not possible. However, one can fine tune lithium intercalating anodes possessing the said properties by way of manipulating the physical properties, which in turn could be achieved by adopting suitably designed synthesis protocol. Approaches to construct structures such as mesoporous,[1,2] hollow spheres,[3,4] nanospheres,[5] nanowires,[6] nanoplatelets,[7] nanorods,[8] nanosheets,[9] nanocages,[10] nanotubes[11] *etc*. are reported. Of the known structures, micro/nanocubes are rarely reported, due to the requirement of stringent synthesis conditions to obtain the final product in the form of regularly shaped cubes.

Apart from the well-known advantages of nanostructured electrode materials, the associated disadvantages such as low density and high risk of surface side reactions could be addressed,[12] especially when such electrode materials are prepared in the form of a composite consisting of micro/nano architecture. Herein, the micron sized particles offer advantages to offset the critical issues related to nanostructured electrode material. In addition, synergetic advantages of integral microstructure and short diffusion length of the nanoparticles could be achieved in the final product.

Considering the development of alternative anodes for graphite, transition metal oxides including MnO,[13] CoO,[14] Fe$_2$O$_3$,[15] CuO,[16] Cu$_2$O,[17] and NiO[18] have been studied for application in lithium-ion batteries. Among the transition metal oxides, manganese oxide anodes (MnO, MnO$_2$, Mn$_2$O$_3$ and Mn$_3$O$_4$) are of great interest for reasons such as natural abundance, economically viable and environmentally benign nature of manganese. Particularly, Mn$_2$O$_3$ assumes importance due to the high theoretical capacity (1018 mA h g^{-1}) and lower operating voltage (discharge voltage is 0.5 V and charge voltage is 1.2 V) benefits.

Mn$_2$O$_3$ could be prepared in the form of spheres, cubes and plates by adopting methods such as solvothermal, precipitation and polyol solution respectively.[19,20,21] Quite different from

such approaches and from the recent reports on the synthesis of Mn_2O_3 cubes, requiring a structure directing group,[22] the present study discusses on the possibility of adopting a simple co-precipitation method with a specific control on the speed of addition of $(NH_4)HCO_3$ precursor to prepare Mn_2O_3 cubes containing micro/nanostructured particles. These Mn_2O_3 micro/nanostructured cubes are subsequently modified as composites by incorporating an economically viable carbon, *viz.,* cooked rice derived carbon (CRC) as the composite additive. Despite the number of reports available on the different types of carbon exploited for the said purpose, the study explores the possibility of exploiting carbon, derived from the wasted cooked rice as a compositing additive to improve the electrochemical behavior of pristine Mn_2O_3 cubes.

Rice, a popularly known carbohydrate, rich in carbon content has been made cheap, especially in India due to government policies. Besides edible purpose, rice starch finds its application in textile industry [23] and acts as an energy efficient fuel [24] to prepare wide variety of ceramics,[25] semiconducting and electrochemically active electrode materials.[26] However, rice being the major component of South Indian food item, especially after cooking, gets wasted in larger quantities from restaurants, hostels and community halls, apart from domestic wastage at home. Such a waste material, considered to be unfit for any other purpose has been collected and processed to obtain CRC through a filth-to-wealth attempt, that has further been deployed as a composite material to possibly improve the electrochemical performance of Mn_2O_3 cubes, obtained from a simple co-precipitation method without deploying any structure directing additive.

The present study is thus bestowed with twin novelty components, *viz.,* exploration of CRC as a conducting additive to improve the lithium intercalating behavior of Mn_2O_3 microcubes (obtained from nanoflakes) and the optimisation of rate of addition of $(NH_4)HCO_3$ to obtain symmetrically formed Mn_2O_3 cubes. Because, there are reports available only on the effect of concentration of added sulphate (SO_4^{2-}) precursor to prepare $MnCO_3$ spheres[27] and not on the effect of rate of addition of $(NH_4)HCO_3$ precursor to obtain $MnCO_3$ cubes. Herein, we report for the first time about the change in the morphology of Mn_2O_3 final product, which could be tuned as a function of rate of addition of $(NH_4)HCO_3$ precursor. A shift from spheres – nano flakes (with desired thickness) - cubes (*via.* stacking of nano flakes) has been noticed with a change in the rate of addition of $(NH_4)HCO_3$. Role of added CRC, rate of addition of $(NH_4)HCO_3$ precursor, effect of morphology and the optimization of CRC required to improve the electrochemical properties of Mn_2O_3 are discussed in this communication. Of the attempted combinations, Mn_2O_3/CRC-20 anode exhibits superior electrochemical performance, viz. 830 mA h g^{-1} as initial and 490 mA h g^{-1} as progressive capacity up to 100 cycles, resulting from the desirable combination of micro/nanostructure and the regularly formed cubes obtained from systematically stacked Mn_2O_3 nano flakes along with the added CRC.

2. Experimental Section

2.1. Materials and Synthesis

2.1.1. Preparation of Mn_2O_3

Deionized (DI) water has been used throughout the experiment. Initially, manganese carbonate microcubes were prepared by co-precipitation method, as follows: $MnSO_4 \cdot H_2O$ (Alfa Aesar), $(NH_4)HCO_3$ (Alfa Aesar) and C_2H_5OH (Alfa Aesar) were used as received, without further purification. Two stock solutions *viz.,* $MnSO_4$ (1.6902 g of $MnSO_4 \cdot H_2O$ in 300 mL of deionized water) and $(NH_4)HCO_3$ (0.7906 g of $(NH_4)HCO_3$ in 300 mL of deionized water) were prepared and to the solution of $MnSO_4$, 30 mL of ethanol was added and stirred until a clear solution is obtained. Subsequently, $(NH_4)HCO_3$ stock solution was added to the above solution at room temperature. Within 2 min, the solution turned to milky white, which is an indication of formation of $MnCO_3$. Then, the solution was stirred continuously for 2 h at room temperature to obtain a blend of milky white and purple colour. $MnCO_3$ microcubes thus obtained were separated from the reaction mixture by centrifugation, and washed several times with DI water and ethanol to remove the impurities. The collected $MnCO_3$ microcubes were dried in hot air oven for 12 h and subjected to further processing. i.e., porous Mn_2O_3 microcubes with nanoflakes were prepared by the thermal treatment of $MnCO_3$ microcubes at 600 °C for 2 h in open atmosphere and at a heating rating of 1 °C min^{-1}. It is noteworthy that no structure directing additive has been deployed to prepare Mn_2O_3 nanocubes, which is the significance of the study. Quite different from conventional approaches, the effect of rate of $(NH_4)HCO_3$ addition in changing the morphology of final product (Mn_2O_3) has been studied. In this regard, 300 mL of $(NH_4)HCO_3$ solution has been added in three chosen rates, *viz.,* 2 h, 3 h and 4 h and the correspondingly formed Mn_2O_3 powders were collected individually and characterised further. From a careful analysis of XRD and SEM, addition of 300 mL of $(NH_4)HCO_3$ in 2 h has been optimized to obtain nanoflakes of desired thickness to produce Mn_2O_3 microcubes of preferred morphology. So, the Mn_2O_3/C composite preparation has been carried out only with the optimized Mn_2O_3 cubes obtained with 2 h addition of $(NH_4)HCO_3$ solution.

2.1.2. Preparation of Cooked Rice Carbon (CRC) and Mn_2O_3/CRC Composite

Waste rice has been collected from a nearby restaurant for preparing CRC. The collected rice was pre-treated in Ar atmosphere at 300 °C for 10 h. The obtained black grains were ground for 30 min and furnace heated at 700 °C for 10 h in Ar atmosphere to obtain CRC.

Mn_2O_3/CRC was prepared by mixing Mn_2O_3 cubes with CRC (10, 20 and 30% ratio), ground for 30 min and subsequently heated in the furnace at 400 °C for 2 h in Ar atmosphere to get better adherence. With a view to understand

the role and to optimise the amount of CRC required to improve the electrochemical performance of pristine Mn_2O_3 microcubes, three different ratios of CRC, *viz.,* 10, 20 and 30 wt% were chosen for the study. The composites obtained as the final product will be represented hereafter as Mn_2O_3/CRC-10, Mn_2O_3/CRC-20 and Mn_2O_3/CRC-30 respectively to represent the addition of 10, 20 and 30 wt% of cooked rice derived carbon to pristine Mn_2O_3 to form the final composite. Such composites were characterised individually to better understand the role of CRC and the extent of improvement observed in terms of electrochemical properties, as a function of added amount of CRC.

3. Physicochemical Characterization

The crystal structure information of the synthesized compound was analysed with Bruker D8 Advance X-ray diffraction using Ni-filtered Cu Kα radiation (λ = 1.5406 Å). Fourier transform infrared spectroscopy (FT-IR) studies were carried out using Bruker Tensor 27 FT-IR Spectrometer. By using a TA instrument SDT Q600 thermogravimetric analyser, TGA studies were carried out. To study the particle size, surface morphology and the presence of carbon coating, Scanning electron microscopy (SEM, JEOL JSM6480LV system), Field emission scanning electron microscopy (FESEM, Gemini) and Transmission electron microscopy (TEM, Tecnai 20 G2 (FEI make)) were used. The chemical composition of the products has been obtained from X-ray photoelectron spectroscopy (XPS, MULTILAB 2000 Base system with X-Ray, Auger and ISS attachments). The surface area and the pore size of the samples were determined by Brunauer- Emmett- Teller (BET) method by nitrogen adsorption/ desorption using Quantachrome, NOVA version 11.02. VMP3 multichannel potentiostat- galvanostat system (Biologic Science Instrument) was used to study the cyclic voltammetry (CV) in the potential window of 0.01-3.0 V and at a scan rate of 0.1 mV s^{-1}. Charge-discharge cycling studies were performed with Arbin cycler.

4. Electrochemical Characterization

The electrochemical measurements were carried out using CR2032 type coin cells, wherein copper foil has been used as the current collector and lithium metal as counter and reference electrode. A solution consisting of 1.0 M $LiPF_6$ dissolved in 1:1 (v/v) mixture of ethylene carbonate (EC)/ dimethyl carbonate (DMC) serves as the electrolyte. The working electrode was fabricated by mixing Mn_2O_3 microcubes as the active material, conductive carbon (Super-P) and polyvinylidene fluoride binder in the weight ratio of 70: 20: 10. Using N-methyl-2-pyrrolidone as solvent, the mixture was made as slurry and coated on copper foil. The coated electrode was dried in oven at 80 °C to evaporate NMP, hot roll pressed to ensure better adherence and cut in to circular discs of 15.5 mm diameter to act as anode in the coin cell assembly.

5. Results and discussion

5.1. Physical Characterisation of Mn_2O_3 cubes obtained from $MnCO_3$ nanoflakes and the formed Mn_2O_3 /CRC composite

From Scheme 1, it is evident that the added $(NH_4)HCO_3$ with an optimum speed (300 mL/2 h) reacts with $MnSO_4$ (a) to form $MnCO_3$ flakes (b), which in turn stacks together in a
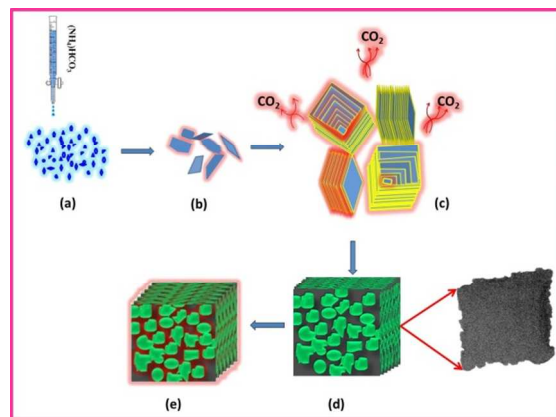
Scheme 1. Synthesis of Mn_2O_3 microcubes with CRC and the corresponding composite with CRC.
a) Precursor $(MnSO_4 + (NH_4)HCO_3)$ b) Flakes of $MnCO_3$, c) $MnCO_3$ cubes, d) Mn_2O_3 cubes e) Mn_2O_3/CRC composite.

symmetrical manner to form $MnCO_3$ cubes (c) (Electronic Supplementary Information(ESI), Fig. S1). The cubes thus obtained release CO_2 gas upon furnace heating at 600 °C for 2 h to produce Mn_2O_3 cubes (d) formed out of Mn_2O_3 nanoflakes. Further, Mn_2O_3/CRC composite is obtained when Mn_2O_3 cubes are heated with CRC at 400 °C for 2 h in Ar atmosphere (e).
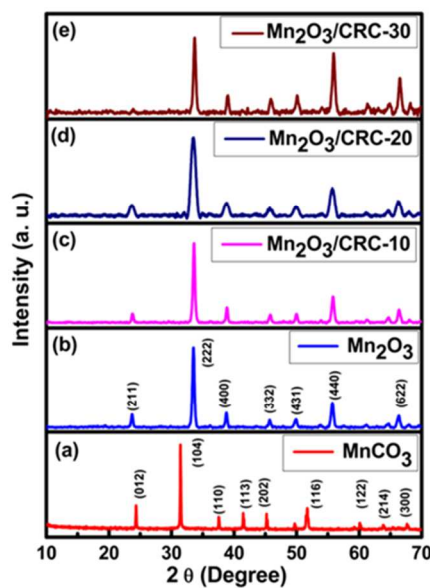
Fig. 1 XRD pattern of $MnCO_3$, Mn_2O_3 and composites of Mn_2O_3 with CRC

X-ray diffraction (XRD) measurements were carried to understand the structure and phase of the precursor and the final product obtained as per Scheme 1. Fig. 1 shows the XRD pattern of $MnCO_3$, Mn_2O_3 and Mn_2O_3/CRC composites. Fig. 1a shows the diffraction peaks of $MnCO_3$, wherein all the peaks could be indexed to the rhodochrosite structure with $R\bar{3}c$ space group, as per JCPDS card No. 86-0172. The lattice constant values are a = 4.78 and b = 15.61. No impurity peaks are observed and from this, one can understand that high purity $MnCO_3$ powder has been formed out of this synthesis. Fig. 1b represents the XRD pattern of Mn_2O_3 powder, which shows striking similarity with the cubic Mn_2O_3 (JCPDS card No. 01-1061) product.

As there are no peaks corresponding to $MnCO_3$ powder, it is understood that complete decomposition of $MnCO_3$ has taken place to form phase pure Mn_2O_3. Fig. 1c-e corresponds to the XRD of Mn_2O_3/CRC composite products, wherein the presence of sharp and strong peaks confirms the crystallinity of the final product obtained. Among the three composites, Mn_2O_3/CRC-10 shows no change in the XRD pattern, peak position and intensity. However, Mn_2O_3/CRC-20 exhibits slightly broader bragg peaks, thus indicating the nanocrystalline product formation, aided by the increased carbon content. On the other hand, Mn_2O_3/CRC-30 shows diminished (211) peak at 2θ = 23.7° and slightly enhanced intensity for peaks located at 2θ = 61.3° and 64.8°, which is considered as a deviation from the standard pattern. As a result, one can deduce the information that Mn_2O_3/CRC-20 provides interesting bragg behavior, leaving behind some scope to consider the same as a better composition, compared with the rest of the composites.

Interestingly, the XRD pattern of CRC (ESI, Fig. S2a) contains two broad peaks at 2θ ranging from 20 to 28° and at 2θ = 44°, corresponding to the (002) and (101) planes, thus representing the graphitic stacking pattern of carbon. Hence, it is presumed that CRC might possess high electrical conductivity. Further, Raman spectrum of CRC shows two peaks at 1350 and 1580 cm^{-1} corresponding to the defect (D) and graphitic band (G) (ESI, Fig. S2b), which could be ascribed to the vibrations of carbon atoms with sp^2 electronic configuration. [28, 29] The G band is found to be narrow and exhibits slightly higher intensity than the corresponding D band, thus confirming the possibility that CRC possesses low graphitization degree.[30] In other words, I_D/I_G ratio is 0.86, which indicates that small amount of defects are present in the sample. Raman spectrum of Mn_2O_3/CRC-20 composite (ESI, Fig. S3) consists of a high intensity peak at 658 and low intensity peaks at 580 and 478 cm^{-1}, which is an indication of the formation of Mn_2O_3 possessing well defined electronic states.[31,32]

Fig. 2 depicts the TG analysis of the formed intermediate product *viz.,* $MnCO_3$ nanoflakes and Mn_2O_3/CRC-20 obtained as the final product. According to the TGA curve, it is evident that 405 °C is the decomposition temperature of $MnCO_3$ to form Mn_2O_3. In Fig. 2a, two weight loss regions corresponding to 150 and 405 °C are seen. The weight loss around 150 °C is caused due to the removal of water from the sample. The

subsequent and drastic weight loss around 405 °C is ascribed to the thermal decomposition of $MnCO_3$ to form Mn_2O_3, by the evolution of CO_2 and MnO.[33,34] In Fig. 2b, the first weight loss at 150 °C is due to the removal of water/moisture from CRC and the second weight loss in the 370-530 °C region is due to the carbon from CRC present in the Mn_2O_3/CRC composite.
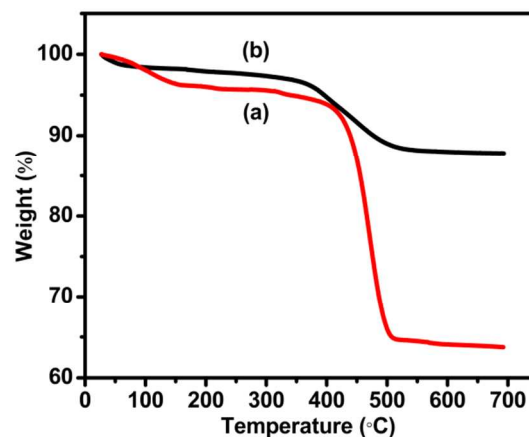
Fig. 2 TGA of (a) $MnCO_3$ and (b) Mn_2O_3/CRC-20 composite

To further understand the local cation arrangement of $MnCO_3$ and Mn_2O_3 microcubes, FT-IR was recorded and the results are spectacle in Fig. 3. $MnCO_3$ shows peaks at 2480, 1398, 860 and 717 cm^{-1}, which are attributed to the C-O bending vibration of carbonates (Fig. 3a).[35] FT-IR signature recorded for Mn_2O_3 is displayed in Fig. 3b, wherein carbonate peaks of $MnCO_3$ are not found and the observed peaks are matching with the title compound Mn_2O_3.[36] The presence of three peaks around 514, 578 and 682 cm^{-1} may be attributed to Mn-O and hence the formation of $MnCO_3$ and Mn_2O_3 could be understood.[37]
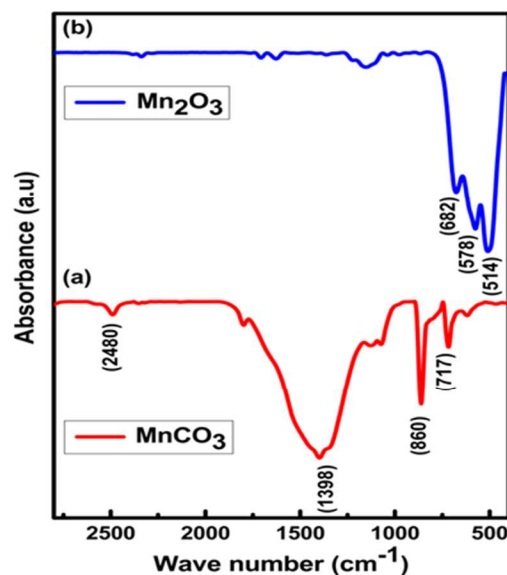
Fig. 3 FTIR spectra of $MnCO_3$ and Mn_2O_3
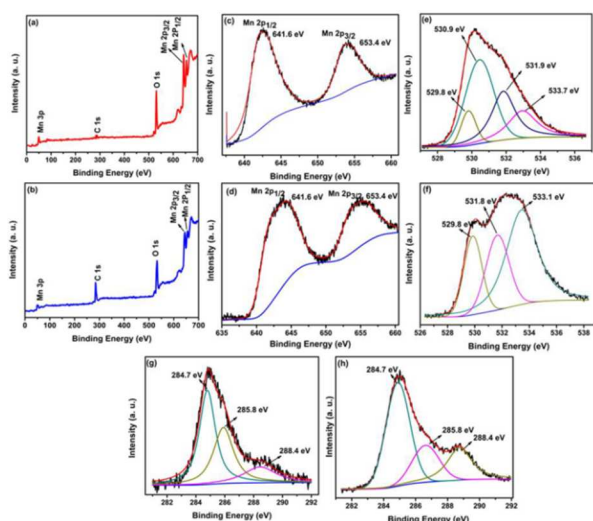
Fig. 4 XPS spectra of bare Mn_2O_3 and $Mn_2O_3/CRC-20$ composite; (a-b) Survey spectrum, (c-d) Mn 2p, (e-f) O 1s and (g-h) C 1s spectrum

XPS is one of the best implements to identify the elemental composition and chemical bonding of the formed material. Fig. 4a and b represent the XPS survey spectra corresponding to those of Mn_2O_3 microcubes and Mn_2O_3/CRC composite, wherein four main peaks located at 284.7 , 531.3 , 641.9 and 653.7 eV, pertinent to elements such as C 1s, O 1s, Mn $2p_{3/2}$ and Mn $2p_{1/2}$ respectively are seen. Fig. 4c and d exhibit the deconvoluted XPS spectra of the Mn 2p, wherein two peaks located at 641.6 and 653.4 eV are attributed to Mn $2p_{3/2}$ and Mn $2p_{1/2}$, and the corresponding spin energy separation of 11.8 eV is matching with that of Mn_2O_3.[38] O 1s spectrum shows four peaks after deconvolution and are positioned at 529.8, 530.9, 531.9 and 533.7 eV in Fig. 4e and f. Such peaks could be assigned to the presence of oxygen in the binary oxide.[39,40,41] The peaks of C 1s are attributed to graphitized carbon and some O-C bonds are placed at 284.7, 285.8 and 288.4 eV.[42] The recorded EDX spectrum confirms the presence of Mn and O in Mn_2O_3 and the presence of carbon along with Mn and O in the composite (ESI, Fig. S4), thus substantiating the chemical composition and stoichiometry of the chosen Mn_2O_3 and its corresponding composite with CRC. The percentage composition of elements present in $Mn_2O_3/CRC-20$ clearly evidences the carbon content as 19.5, which is in agreement with the CRC-20 composite (ESI, Inset of Fig. S4b).

To study the morphology and particle size of $MnCO_3$ (intermediate) and the final product, viz. Mn_2O_3, scanning electron microscopy (SEM) was recorded to capture the respective images. Typical images of the $MnCO_3$ intermediate evidence the formation of perfect cubes with 2 µm size (ESI, Fig. S1). Thermal decomposition of $MnCO_3$ forms Mn_2O_3 and the morphological features (Fig. 5) correspond to the presence of cubes, obtained from the systematic stacking of nanoflakes. Fig. 5a shows low magnification images of Mn_2O_3, wherein more or less uniform size and shape of cubes are seen. Fig. 5b,

c and d are high magnification images of Mn_2O_3, in which formation of symmetrical and individual cubes with an edge length of approximately 1.5 to 2.0 µm is evident. Systematic stacking of nanoflakes in a uniform manner with an inherent control (induced by the selected synthesis protocol) over the thickness and length spontaneously produces symmetrically formed Mn_2O_3 microcubes without any agglomeration, which is noteworthy. The shape and size of the Mn_2O_3 cubes are greatly influenced by the rate of addition of $(NH_4)HCO_3$ solution to the $MnSO_4 \cdot H_2O$ precursor solution and by the concentration of SO_4^{2-}.
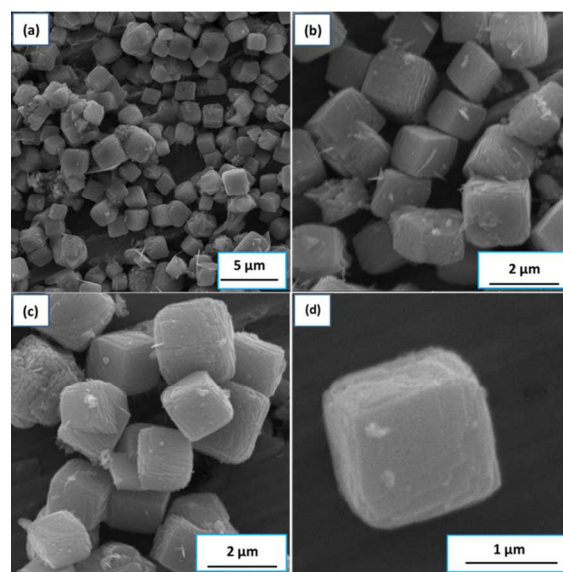
Fig. 5 (a) Low magnification and (b-d) high magnification SEM images of Mn_2O_3 microcubes
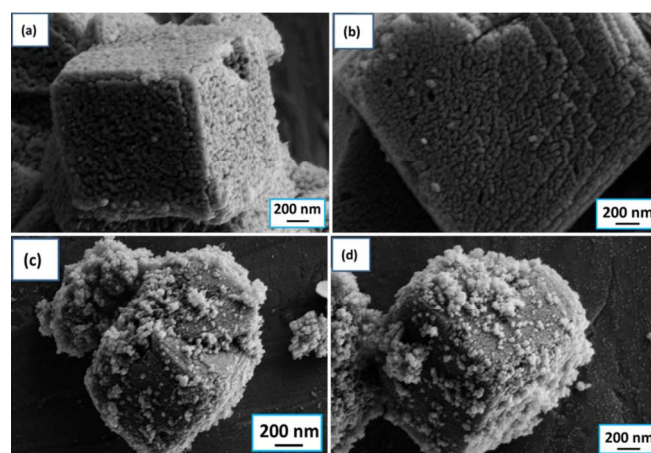
Fig. 6 FESEM images of (a-b) pure Mn_2O_3 and (c-d) $Mn_2O_3/CRC-20$ composite

The significant role of rate of addition of $(NH_4)HCO_3$ in deciding the morphology of (ESI, Fig. S5) the final product in an indispensable manner could be understood from the following. The addition of $(NH_4)HCO_3$ solution (300 mL) in 30 min results in the formation of $MnCO_3$ and Mn_2O_3

microspheres (ESI, Fig. S5a), whereas an addition time of 2 h results in the formation of desired Mn_2O_3 microcubes containing properly stacked nanoflakes by allowing the existence of individual microcubes (ESI, Fig. S5b). On the other hand, an addition time of 3h leads to the formation of nanoflakes with increased thickness (55 nm), due to which, the Mn_2O_3 cubes have a tendency to undergo slight agglomeration (ESI, Fig. S5c). The same is clearly evidenced in Fig. S5d with highly agglomerated Mn_2O_3 particles obtained with the addition of $(NH_4)HCO_3$ in 4h. As a result, coalesced cubes of Mn_2O_3 have been obtained, especially when the addition time exceeds 2 h. Hence, it is understood that the carefully chosen concentration (0.03 M) of $(NH_4)HCO_3$ needs to be added in an optimized time period of 2 h to obtain discrete cubes with desired thickness, edges and porosity.

Fig. 6 presents the FESEM images of the as-prepared pure Mn_2O_3 (a-b) and the composite of Mn_2O_3 obtained with 20% CRC powder (c-d). Fig. 6a represents the low magnification image of pure Mn_2O_3, wherein assembly of perfectly formed cubes from nanoparticles, possessing a size of around 30-50 nm, have been obtained, which is in agreement with the findings from transmission electron microscopy (TEM). In the high magnification image, it is clearly seen that a single Mn_2O_3 microcube contains symmetrically packed nanoflakes and the flakes are formed out of irregularly shaped nanoparticles that bridge with each other to realize a flake thickness of 35-45 nm, as seen in Fig. 6b. Fig. 6c and d are low and high magnification FESEM images of Mn_2O_3/CRC-20 composite respectively. Presence of carbon coating on Mn_2O_3 microcubes is obvious from the images, which are further substantiated by TEM results. Such a carbon coating is highly essential to provide better electronic conductivity through carbon wiring.
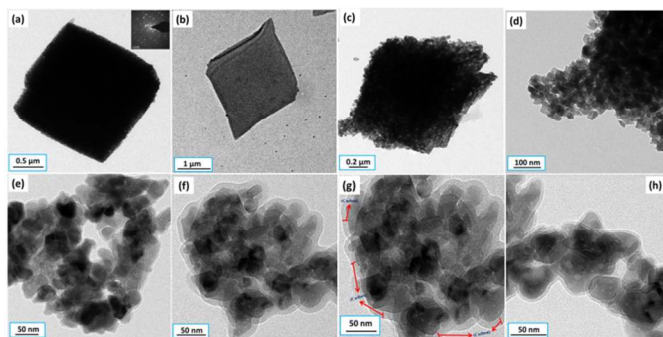
Fig. 7 TEM images of (a-d) pristine Mn_2O_3 and (e-h) Mn_2O_3/CRC-20 composite

TEM images evidence the presence of cubes (Fig. 7a), formed out of nanoflakes (Fig. 7b) containing systematically grouped assembly of irregularly shaped nanoparticles of 30-50 nm size (Fig. 7c and d with a closer view). The presence of carbon coating (grey colour) found on the surface of individual Mn_2O_3 cubes is clearly seen in Fig. 7e and f. Existence of individual Mn_2O_3 cubes possessing a thin line of carbon coating to avoid agglomeration and to restrict/partially allow the unavoidable volume expansion is seen in the zoomed image of

Fig. 7f (Fig. 7g). Similarly, presence of continuous chain like carbon network arrangement, otherwise known as carbon wiring of Mn_2O_3/CRC composite is evident from Fig. 7h. Closer view of TEM images of Mn_2O_3 nanoflakes is illustrated in Fig. S6 (a-d), which confirms the fact that the microcubes are built with the symmetrically formed nanoflakes. SAED pattern evidences the presence of irregular diffraction spots, corresponding to the presence of polycrystalline phase of bare Mn_2O_3 (Inset of Fig. 7a). The surface area and porous structure of Mn_2O_3 and the corresponding Mn_2O_3/CRC-20 composite have been investigated by nitrogen isotherm adsorption-desorption measurement (ESI, Fig. S7). The Brunauer-Emmett-Teller (BET) surface area of Mn_2O_3/CRC-20 composite is measured to be 67.9 m^2g^{-1}, which is higher than that of Mn_2O_3 microcube (26.8 m^2g^{-1}). The high surface area of the composite is associated with the presence of mesoporous particles, which in turn facilitates facile electrolyte accessibility, rapid lithium ion diffusion and buffering of volume expansion.[43] Interestingly, Type-IV isotherm has been obtained, wherein the pore-size distribution for Mn_2O_3 microcube (46.2 nm) and Mn_2O_3/CRC-20 composite (38.1 nm) are shown in the inset of Fig. S7 a and b, indicating the presence of mesopores in the chosen products. Due to the presence of larger pores with open windows, CRC finds an easy access to the pores and forms a conducting carbon network in Mn_2O_3/CRC-20 composite, thus increasing the scope for improved performance of Mn_2O_3/CRC-20 electrode.[44]

5.2 Electrochemical Characterization of pristine Mn_2O_3 and Mn_2O_3/CRC-20 composite anodes
Cyclic Voltammetry
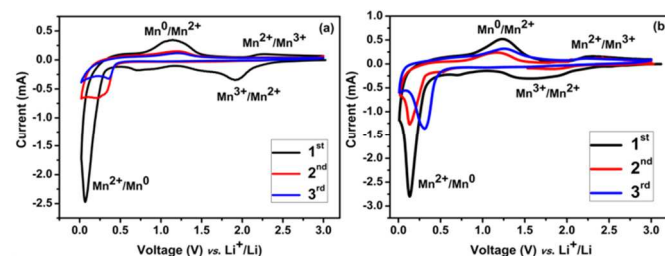
Fig. 8 Cyclic voltammogram of (a) Bare Mn_2O_3 and (b) Mn_2O_3/CRC-20 composite anode recorded at a scan rate of 0.1 mVs^{-1} in the range of 0.01-3.0 V *versus* Li^+/Li

Fig. 8 shows the cyclic voltammetry of pristine Mn_2O_3 and Mn_2O_3/CRC-20 composite anodes recorded at a scan rate of 0.1 mV s^{-1} in the voltage range of 0.01 to 3.00 V at room temperature. Actually, three reduction peaks are found in the cathodic side in the first cycle and it is quite different from the subsequent cycles, which is not unusual.[45] A broad peak located at 1.35 V in the cathodic process is due to the reduction of Mn^{3+} to Mn^{2+}. The second peak is located at 0.65 V, which could be ascribed to the decomposition of solvent from the electrolyte to form solid electrolyte interface (SEI). In addition to the said peaks, the main and high intensity peak observed at 0.21 V is attributed to the reduction of Mn^{2+} to Mn^0. Similarly, the anodic

process of the same cycle contains two visible peaks at 1.25 and 2.32 V, which are attributed to the oxidation of Mn^0 to Mn^{2+} and Mn^{2+} to Mn^{3+} respectively.[46] However, the cathodic peak current and the related integrated area of the second cycle are found to get reduced when compared with the initial cycling performance, which is an indication of irreversible capacity loss taking place during the process. However, from the second cycle onwards, the peak current is found to be almost the same in the subsequent cycles, but a small shift in peak position, say 0.26 V have been observed.[46] For the above described observation, the following equations hold good and justify the lithium insertion and extraction processes related to micro/nanocubes of Mn_2O_3.[45,47,48]

$$2Li^+ + 3Mn_2O_3 + 2e^- \rightarrow 2\ Mn_3O_4 + Li_2O \qquad (1)$$

$$2Li^+ + Mn_3O_4 + 2e^- \rightarrow 3MnO + Li_2O \qquad (2)$$

$$2Li^+ + MnO + 2e^- \leftrightarrow Mn + Li_2O \qquad (3)$$

$$Mn + x\ Li_2O \leftrightarrow 2x\ Li^+ + MnOx + 2x\ e\ (1.0 < x < 1.5) \qquad (4)$$
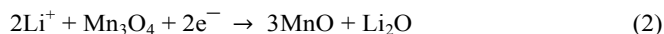
Upon comparison, the larger area and the increased peak current value exhibited by the cyclic voltammetry behavior of Mn_2O_3/CRC-20 anode indicates the beneficial effect of added CRC in improving the lithium intercalation/de-intercalation

behavior with respect to pristine Mn_2O_3 anode.[49-51] Since parameters such as nanoflakes and microcubes are commonly associated with both the anodes, the observed improvement in electrochemical properties is attributed to the advantageous effect of CRC in increasing the conductivity and facilitating the faster diffusion of lithium ions.

Charge-discharge Cycling

Fig. 9a illustrates the cycling performance of the bare and composite of Mn_2O_3 anode using galvanostatic technique. The micro/nano Mn_2O_3 cubes as anode shows a capacity value below 100 mA h g^{-1}, especially after 20 cycles, mainly due to the inferior conductivity values associated with pristine Mn_2O_3, as there are no interconnection between nanoparticles and/or nanoflakes. But, the Mn_2O_3/CRC-20 composite anode shows a capacity as high as 490 mA h g^{-1} at 50 mA g^{-1} even after 100 cycles. Similarly, the better cycling stability of Mn_2O_3/CRC-20 than pristine Mn_2O_3 anode could be attributed to the presence of conducting carbon network between the nanoparticles and nanoflakes of the composite, aided by the added CRC. The same has been clearly evidenced from TEM and FESEM results. Mn_2O_3/CRC-20 anode shows better capacity than the bare and the remaining two composites viz., Mn_2O_3/CRC-10 and Mn_2O_3/CRC-30 anode. The insufficient coverage of anode active material in the 10 wt% CRC and the exceeding thickness
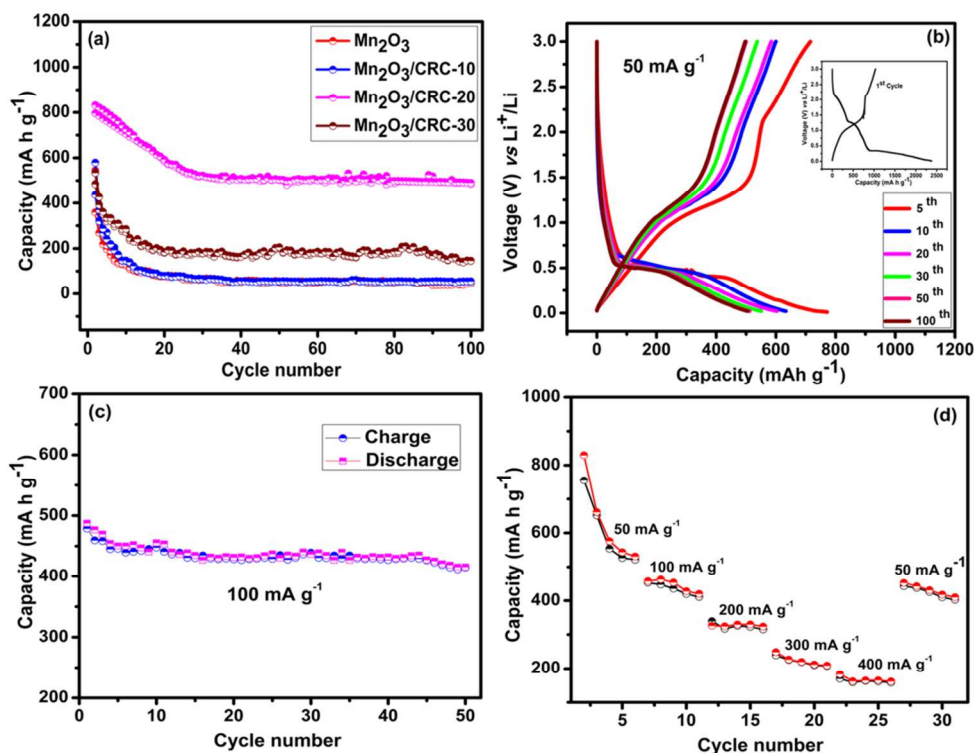
Fig. 9 (a) Cycling performance of pristine Mn_2O_3 anode and Mn_2O_3/CRC anodes (CRC-10, CRC-20, CRC-30) at a current density of 50 mA g^{-1} and (b) Discharge-charge profile of Mn_2O_3/CRC-20 anode at a current density of 50 mA g^{-1} (c) Extended cycle life behavior Mn_2O_3/CRC anode under the influence of 100 mA g^{-1} and (d) Rate capability of Mn_2O_3/CRC-20 anode in the voltage range of 0.01-3.00 V versus Li$^+$/Li.

of 30 wt% CRC that impedes the easy penetration of lithium ions pertinent to Mn_2O_3/CRC-30 anode are believed to be the reasons of realization of inferior capacity compared with that of Mn_2O_3/CRC-20 anode.

Fig. 9b displays the discharge and charge profile of Mn_2O_3/CRC-20 anode in the voltage range of 0.01 to 3.00 V with a current density of 50 mA g^{-1}. The first discharge and charge capacity values are 2380 and 1084 mA h g^{-1} respectively, wherein a small portion of discharge capacity is obtained during the continuous decrease in the open circuit potential up to 1.35 V, which could be related to the reaction of Mn_2O_3 to form Mn_3O_4, as mentioned in equation (1). The voltage then decreases to ~ 0.34 V with the appearance of a new plateau. This may be attributed to the reduction of Mn_3O_4 to MnO, as expressed in equation (2). The voltage further decreases gradually down to a deep discharge limit of 0.01 V, when the phase transformation reaction is taking place with the complete reduction of MnO to Mn and formation of Li_2O, as per equation (3) (Inset of Fig. 9b). It is to be mentioned here that the first total discharge capacity is 2380 mA h g^{-1}, which is twice the theoretical capacity of Mn_2O_3 (1018 mA h g^{-1}). Probable reason for the realization of excess capacity could be related to the decomposition of the electrolyte at a lower voltage and the generation of a solid electrolyte interface (SEI) layer, wherein lithium storage takes place by interfacial charging at the metal/Li_2O interface.[52-54,37] Upon careful investigation of the first charge profile, a curve found at the voltage range from 1.0 to 1.4 V is associated with the oxidation of Mn to MnO. Subsequently, MnO reacts with Li_2O, when the electrode potential exceeds 2.1 V and forms a mixture of MnO and MnO_x (1.0 <X<1.5) expressed by equation (4). Based on this mechanism, Mn_2O_3/CRC-20 anode exhibits an appreciable second cycle capacity of 831 mA h g^{-1}, (Fig. 9b) 50th cycle capacity of 505 mA h g^{-1} and a progressive steady-state capacity of 490 mA h g^{-1} at 50 mA g^{-1}, even after completing 100 cycles. The corresponding coulombic efficiency behavior also increases from 43.5 to 99.9 %, which is noteworthy. Similarly the cycling performance of Mn_2O_3/CRC-20 anode under a current density of 100 mA g^{-1} is also encouraging, wherein an appreciable capacity of 450 mA h g^{-1} has been obtained even after 50 cycles, which is higher than the reported results.[55]

Rate capability and Electrochemical Impedance Spectroscopy (EIS) studies

The rate capability of Mn_2O_3/CRC-20 anode under the influence of different current densities is shown in Fig. 9d. As expected, specific capacity decreases at higher current densities in such a manner that a capacity of 457 mA h g^{-1} has been observed at 100 mA g^{-1} and 183 mA h g^{-1} at 400 mA g^{-1}. When the current density was decreased to 50 mA g^{-1}, the capacity gets improved to 452 mA h g^{-1} and resumes the original capacity. Hence, the study demonstrates that Mn_2O_3/CRC-20 anode has better capacity retention and good cycleability

performance. Such a performance of this material could be attributed to the presence of nanoflakes which are interconnected with CRC. This is the ever first report on CRC to endorse and to improve the lithium intercalating behavior of Mn_2O_3 cubes as anode.
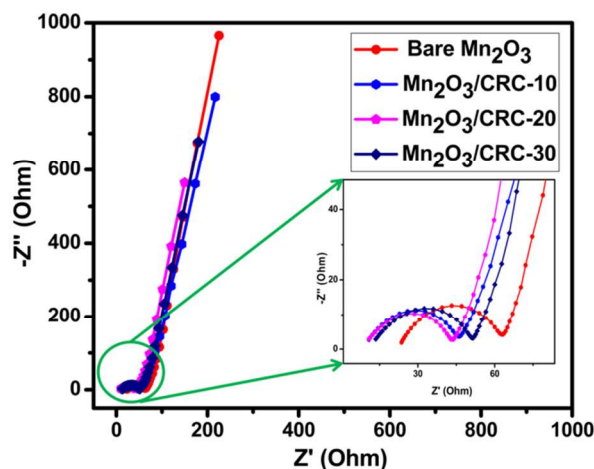
Fig. 10 Electrochemical Impedance Spectroscopy behavior of cells containing pristine Mn_2O_3 anode and Mn_2O_3/CRC anodes consisting of 10, 20 and 30 wt.% CRC

Electrochemical Impedance Spectroscopy (EIS) was performed to understand the effect of added CRC in improving the conductivity as well as the lithium transport kinetics of Mn_2O_3/CRC composites (in comparison with that of pristine Mn_2O_3 anode) as a function of concentration of carbon. Electrochemical Impedance behavior of the cells was measured in the frequency range of 10 kHz to 100 mHz. Figure 10 shows the comparison of impedance behavior of bare Mn_2O_3 and Mn_2O_3/CRC composites measured at the open circuit voltage of the as fabricated cell. From the inset of Figure 10, it is evident that the high frequency semicircle, attributed to the solid electrolyte interface film formation and/or contact resistance (R_s) corresponding to that of Mn_2O_3 anode exhibits high contact resistance compared with the composites $viz.$, Mn_2O_3/CRC-10, 20 and 30 individually. The middle frequency of the semicircle due to the charge transfer resistance on the electrode and electrolyte interface (R_{ct}), of Mn_2O_3/CRC-20 composite is found to be lower than the remaining composites and that of pristine Mn_2O_3 (Table-I). This could be understood in terms of the increased contact area benefit, resulting from the presence of nanocrystalline particles and the enhanced electrical conductivity of Mn_2O_3/CRC-20 electrode. At the low frequency region, corresponding to the diffusion of lithium ions within the electrode material, more or less straight line behavior is observed for Mn_2O_3/CRC-20 composite, compared with the remaining anodes, thus evidencing the faster diffusion of lithium-ions, as understood from the charge/discharge studies also. As mentioned already, the absence of carbon (pristine

Anode	R_s (Ω)	R_{ct} (Ω)
Pristine Mn_2O_3	23.6	39.5
Mn_2O_3/CRC-10	10.8	35.4
Mn_2O_3/CRC-20	10.8	32.6
Mn_2O_3/CRC-30	13.5	38.3

Table. I Contact resistance (R_s) and Charge transfer resistance (R_{ct}) of pristine Mn_2O_3 anode and Mn_2O_3/CRC anodes consisting of 10, 20 and 30 wt.% CRC

Mn_2O_3), lesser carbon with ineffective carbon wiring (Mn_2O_3/CRC-10) and higher carbon content than the optimum amount that impedes the facile diffusion of lithium ions (Mn_2O_3/CRC-30) are responsible individually for the currently observed higher internal resistance values, which are ultimately responsible for the inferior electrochemical properties compared with that of Mn_2O_3/CRC-20 anode.[44, 56-59]

6. Conclusion

Mesoporous Mn_2O_3 microcubes containing stacked nanoflakes composed of nanoparticles with irregular shape have been prepared without adding any surfactant. In order to impart value addition to the currently prepared Mn_2O_3 microcubes, a cheaper carbon additive, obtained from wasted cooked rice has been used to prepare Mn_2O_3/CRC composite. Optimized rate of addition of $(NH_4)HCO_3$ (300 mL/2 h), deployment of optimum concentration of CRC (20 wt%) and the presence of micro/nanostructure to admit the anticipated volume expansion and enhanced lithium diffusion kinetics in synergy have offered facile transportation of lithium ions and to recommend Mn_2O_3/CRC-20 as a better performing anode. An initial capacity of 830 mA h g^{-1} and a reasonable capacity of 490 mA h g^{-1} up to 100 cycles have been exhibited by Mn_2O_3/CRC-20 anode, when discharged at 50 mA g^{-1}. The anode finds its suitability at various fairly high current densities also. The exploitation of symmetric Mn_2O_3 cubes for lithium battery application fetches interest to the composite and the synthesis protocol, apart from the application point of view.

Acknowledgements

Notes

[a]CSIR-Central Electrochemical Research Institute, Karaikudi-630 006, Tamilnadu, India.

[b]Wayne State University-Department of Mechanical Engineering, Michigan 48202-3902, U.S.A.

E-mail: kalaiselvicecri@gmail.com

Supporting Information

Fig. S1: SEM images of $MnCO_3$ microcubes with nanoflakes, **S2:** XRD and Raman behavior of cooked rice carbon (CRC)**, S3:** Complete Raman spectrum of Mn_2O_3/CRC-20, **S4:** EDX results of the pristine Mn_2O_3 and Mn_2O_3/CRC-20 composite**, Fig. S5** SEM images of Mn_2O_3 obtained by varying the rate of addition of $(NH_4)HCO_3$ precursor, (a) spheres obtained in 30 min, (b) cubes obtained 2 h, (c-d) agglomerated cubes obtained 3 h and 4 h **S6:** Closer view of TEM images of Mn_2O_3 nanoflakes, **S7:** N_2 adsorption-desorption isotherm of (a) Mn_2O_3 and (b) Mn_2O_3/CRC-20 composite

References

1 Y. F. Deng, Z. N. Li, Z. C. Shi, H. Xu, F. Peng and G.H. Chen, *RSC Adv.,* 2012, **2**, 4645– 4647.

2 X. M. Yin, L. B. Chen, C. C. Li, Q. Y. Hao, S. Liu, Q. H. Li, E. D. Zhang and T. H. Wang, *Electrochim. Acta,* 2011, **56**, 2358–2363.

3 J. S. Chen, L. A. Archer and X. W. Lou, *J. Mater. Chem*., 2011, **21**, 9912–9924.

4 F. Zhang, Y. Zhang, S. Y. Song and H. J. Zhang, *J. Power Sources,* 2011, **196**, 8618–8624.

5 Y. Sun, X. Y. Feng, and C. H. Chen, *J. Power Sources,* 2011, **196**, 784−787.

6 K. T. Nam, D. W. Kim, P. J. Yoo, C. Y. Chiang, N. Meethong, P. T. Hammond, Y. M. Chiang and A. M. Belcher, *Science,* 2006, **312**, 885−888.

7 Y. Lu, Y. Wang, Y. Q. Zou, Z. Jiao, B. Zhao, Y. Q. He and M. H. Wu, *Electrochem. Commun.,* 2010, **12**, 101−105.

8 S. Vijayanand, R. Kannan, H. S. Potdar, V. K. Pillai and P. A. Joy, *J. Appl. Electrochem.,*2013, **43**, 995−1003.

9 L. Pan, L. Li and Q. Y. Zhu, *J. Sol.-Gel. Sci. Technol*., 2013, **67**, 573−579.

10 D. Q. Liu, X. Wang, X. B. Wang, W. Tian, Y. Bando and D. Golberg, *Sci. Rep*., 2013, **3**, 2543−2548.

11 J. Xu, L. Gao, J. Y. Cao, W. C. Wang and Z. D. Chen, *Electrochim. Acta,* 2010, **56**, 732−736.

12 A. K. Rai, J. Gim, L. T. Anh and J. Kim, *Electrochim. Acta,* 2013, **100**, 63−71.

13 G. L. Xu, Y. F. Xu, H. Sun, F. Fu, X. M. Zheng, L. Huang, J. T. Li, S. H. Yang and S. G. Sun, *Chem. Commun*., 2012, **48**, 8502−8504.

14 M. Zhang, M. Q. Jia, Y. H. Jin and X. R. Shi, *Appl. Surf. Sci.,* 2012, **263**, 573−578.

15 J. Zhu, Z. Yin, D. Yang, T. Sun, H. Yu, H. E. Hoster, H. H. Hng, H. Zhang and Q. Yan, *Energy Environ. Sci*., 2013, **6**, 987−993.

16 L. L. Wang, H. X. Gong, C. H. Wang, D. Wang, K. B. Tang and Y. T. Qian, *Nanoscale,* 2012, **4**, 6850−6855.

17 D. Q. Liu, Z. B. Yang, P. Wang, F. Li, D. S. Wang and D. Y. He, *Nanoscale,* 2013, **5**, 1917−1921.

18 G. H. Zhang, Y. J. Chen, B. H. Qu, L. L. Hu, L. Mei, D. N. Lei, Q. Li, L. B. Chen, Q. H. Li and T. H. Wang, *Electrochim. Acta,* 2012, **80**, 140−147.

19 L. Hu, Y. K. Sun, F. P. Zhang and Q. W. Xhen, *J. Alloys Compd*., 2013, **576**, 86–92.

20 J. Cao, Yc. Zhu, KY. Bao, L. Shi, SZ. Liu and Y.T. Qian, *J. Phys. Chem. C,* 2009, **113**, 17755–17760.

21 Y. Zhang, Y. Yan, X. Wang, G. Li, D. Deng, L. Jiang, C. Shu and C. Wang, *Chem. Eur. J.,* 2014, **20**, 6126–6130.

22 H.W. Shim, A.H. Lim, K.M. Min and D.W. Kim, *Crys..Eng.Comm.*, 2011, **13**, 6747–6752.

23 J. A. Radley, Industrial Uses of Starch and its Derivatives., *ISBN: 978-94-010-1331-4.*

24 H.B. Goyal, D. Seal and R.C. Saxena, *Renewable and Sustainable Energy Reviews*, 2008, **12**, 504–517.

25 E. Gregorova, W. Pabst and I. Bohacenko, *J. Eur. Ceram. Soc.,* 2006, **26**, 1301–1309.

26 Q-Y. Li, H-Q. Wang, Q-F. Dai, J-H. Yang and Y-L. Zhong, *Solid State Ionics,* 2008, **179**, 269–273.

27 J.B. Fei, Y. Cui, X.H. Yan, W. Qi, Y. Yang, K.W. Wang, Q. He and J. B. Li, *Adv. Mater*., 2008, **20**, 452–456.

28 A. C. Ferrari, J. C. Meyer, V. Scardaci, C. Casiraghi, M. Lazzeri, F. Mauri, S. Piscanec, D. Jiang, K. S. Novoselov, S. Roth and A. K. Geim, *Phys. Rev. Lett.,* 2006, **97**, 187401–187404.

29 A. Maleservic, R. Vitchev, K. Schouteden, A. Volodin, L. Zhang, G. V. Tendeloo, A. Vanhulsel and C. V. Haesendonck, *Nanotechnology,* 2008, **19**, 305604–305609.

30 F. Zhang, K-X. Wang, G-D. Li and J-S. Chen, *Electrochem. Commun.,* 2009, **11**, 130–133.

31 M. C. Bernard, A. H. L. Goff, B. V. Thi and S. C. Detorresi, *J. Electrochem. Soc.,* 1993, **140**, 3065–3070.

32 Q. Javed, F. P. Wang, M. Y. Rafique, A. M. Toufiq, Q. S. Li, H. Mahmood and W. Khan, *Nanotechnology,* 2012, **23**, 415603–415610.

33 Y. Qiao, Y. Yu, Y. Jin, Y-B. Guan and C-H. Chen, *Electrochim. Acta,* 2014, **132**, 323–331.

34 Y.F. Han, L.W. Chen, K. Ramesh, Z.Y. Zhong, F.X. Chen, J.H. Chin and H.W. Mook, *Catal.Today,* 2008, **131**, 35–41.

35 H. Hu, j-y. Xu, H. Yang, J. Liang, S. Yang and H. Wu, *Materials Research Bulletin.,* 2011, **46**, 1908–1915.

36 X. Wang, S. Qiu, G. Lu, C. He, J. Liu, L. Luan and W. Liu. *Cryst.Eng.Comm.,* 2014, **16**, 1802–1809.

37 Y. Cai, S. Liu, X. M. Yin, Q. Y. Hao, M. Zhang and T. H. Wang, *Physica E,* 2010, **43**, 70–75.

38 A. A. Audi, P. M. Sherwood and A.Surf, *Surf. Interface Anal.*, 2002, **33**, 274–284.

39 A. Sakunthala, M. V. Reddy, S. Selvasekarapandian, B. V. R. Chowdari and P. C. Selvin, *Energy Environ. Sci.,* 2011, **4**, 1712–1725.

40 J. Li, S. Xiong, X. Li and Y. Qian, *J. Mater. Chem*., 2012, **22**, 23254–23259.

41 Q. Li, L. Yin, Z. Li, X. Wang, Q. Yongxin and J. Ma, *ACS Appl. Mater. Interfaces,* 2013, **5**, 10975–10984.

42 J-H. Zhou , Z-J. Sui , j. Zhu , P. Li , D. Chen , Y-C. Dai and W-K. Yuan, *Carbon,* 2007, **45**, 785–796.

43 F. Han, L-J. Ma, Q. Sun, Ch. Lei and A-H. Lu, *Nano Res*., 2014, DOI: 10.1007/s12274-014-0531-y.

44 Xi. Fan, J. Shao, Xu. Xiao, L. Chen, X. Wang, S. Li and H. Ge, *J. Mater. Chem. A,* 2014, DOI:10.1039/C4TA01511H.

45 L. Chang, L. Mai, X. Xu, Q. An, Y. Zhao, D. Wang and X. Feng, *RSC Adv.,* 2013, **3**, 1947–1952.

46 Y. F. Deng, Z. E. Li, Z. C. Shi, H. Xu, F. Peng and G. H. Chen, *RSC Adv*., 2012, **2**, 4645–4647.

47 Y. C. Qiu, G. L. Xu, K. Y. Yan, H. Sun, J. W. Xiao, S. H. Yang, S. G. Sun, L. M. Jin and H. Deng, *J. Mater. Chem*., 2011, **21**, 6346–6353.

48 L. Hu, Y. K. Sun, F. P. Zhang and Q. W. Xhen, *J. Alloys Compd*., 2013, **576**, 86–92.

49 A. B. Yuan, S. A. Cheng, J. Q. Zhang and C. N. Cao, *J. Power Sources,* 1999, **77**, 178–182.

50 L. Mai, X. Xu, C. Han, Y. Luo, L. Xu, Y. A. Wu and Y. Zhao, *Nano Lett*., 2011, **12**, 4992–4996.

51 X. Xu, Y. Z. Luo, L. Q. Mai, Y. L. Zhao, Q. Y. An, L. Xu, F. Hu, L. Zhang and Q. J. Zhang, *NPG Asia Mater*., 2012, **4**, e20.

52 X. F. Fang, X. Lu, X. W. Guo, Y. Mao, Y. S. Hu, J. Z. Wang, Z. X. Wang, F. Wu, H. K. Liu and L.Q. Chen, *Electrochem. Commun*., 2010, **12**, 1520–1523.

53 S. Nayak, S. Malik, S. Indris, J. Reedijk and A. K. Powell, *Chem. Eur. J.,* 2010, **16**, 1158–1162.

54 F. L. Wang, J. R. Liu, J. Kong, Z. J. Zhang, X. Z. Wang, M. Itoh and K. I. Machida, *J. Mater. Chem*., 2011, **21**, 4314–4320.

55 M-W. Xu, Y-B. Niu, S-J. Bao and M. Li C. *J. Mater. Chem. A,* 2014, **2**, 3749–3755.

56 S. Yang, H. Song and X. Chen, *Electrochem. Commun.* 2006, **8**, 137–142.

57 A. Leela Mohana Reddy and S. Ramaprabhu, *J. Phys. Chem. C* 2007, **111**, 7727–7734.

58 B. Jin, E.M. Jin, K-H. Park and H-B. Gu, *Electrochem. Commun. 2008*, **10**, 1537–1540.

59 L. Zeng, F. Xiao, J. Wang, S. Gao, X. Ding and M. Wei, *J. Mater. Chem.* 2012, **22**, 14284–14288.